ARTICLE

Check for updates

Hyperfine-structure-resolved laser spectroscopy of many-electron highly charged ions

Naoki Kimura [1✉], Priti[2,3], Yasutaka Kono[2], Pativate Pipatpakorn[2], Keigo Soutome[2], Naoki Numadate [2,4], Susumu Kuma[1], Toshiyuki Azuma [1] & Nobuyuki Nakamura [2]

Hyperfine structures of highly charged ions (HCIs) are favourable spectroscopic targets for exploring fundamental physics along with nuclear properties. Recent proposals of HCI atomic clocks highlight their importance, especially for many-electron HCIs, and they have been theoretically investigated by refining atomic-structure calculations. However, developments in hyperfine spectroscopy of many-electron HCIs have not proceeded due to experimental difficulty. Here, we demonstrate hyperfine-structure-resolved laser spectroscopy of HCIs in an electron beam ion trap plasma, employing the magnetic-dipole transition in the $4d^9 5s$ state of $^{127}I^{7+}$. Ion-state manipulation by controlled electron collisions in the well-defined laboratory plasma enables laser-induced fluorescence spectroscopy of trapped HCIs. The observed spectrum of evaporatively cooled ions under low magnetic fields shows characteristic features reflecting the hyperfine structures. The present demonstration using combined optical and plasma approaches provides a benchmark for state-of-the-art atomic calculations of hyperfine structures in many-electron HCIs, and offers possibilities for a variety of unexploited experiments.

[1] Atomic, Molecular and Optical Physics Laboratory, RIKEN, Saitama 351-0198, Japan. [2] Institute for Laser Science, The University of Electro-Communications, Tokyo 182-8585, Japan. [3] Present address: National Institute for Fusion Science, Toki, Gifu 509-5292, Japan. [4] Present address: Komaba Institute for Science, The University of Tokyo, Tokyo 153-8902, Japan. ✉email: naoki.kimura@riken.jp

Nuclear electron interactions induce particularly small splitting in atomic energy levels, defined as hyperfine structure. Spectroscopically investigating hyperfine structures reveals highly valuable information related to nuclear properties and atomic structures[1]. Extension of the spectroscopic target, from the usually studied neutral atoms or singly charged ions to highly charged ions (HCIs), represents an excellent approach to enhance hyperfine interactions owing to contracted electron clouds. Spectroscopic measurements of hyperfine structures in few-electron HCIs, such as H-, He-, Li-, and Be-like ions, have been widely performed by taking advantage of their large hyperfine splittings. They have successfully contributed to tests of relativistic and quantum electrodynamics (QED) atomic theories as well as investigations of nuclear properties[2–14].

In contrast to few-electron HCIs, hyperfine spectroscopy of many-electron HCIs provides distinctive examples to gain a deeper understanding about complex relativistic electron correlations. Nevertheless, this implicates considerable experimental challenges as high spectral resolution (i.e., better than their slightly enhanced hyperfine structure) is required. Such HCIs have recently attracted much attention, triggered by proposals for their application in high-precision atomic clocks. HCI clocks are expected to be a sensitive probe for time variations of the fine-structure constant α for testing modern physical theories beyond the Standard Model[15]. A number of candidates for HCI clocks have been proposed[16–31], and their transition wavelengths have been experimentally investigated[32–35]. Micke et al. recently demonstrated quantum logic spectroscopy of HCIs using Ar^{13+}, which has no hyperfine structure, promising realization of the HCI clocks[36,37]. For further HCI atomic clock development employing fascinated transitions highly sensitive to the α variation[15], it is necessary to gain a better understanding of hyperfine structure in many-electron heavy HCIs with a nuclear spin. The atomic-structure calculations have been developed to provide hyperfine-structure constants[38–42], and several theoretical studies suggested that hyperfine interactions in promising HCI clock candidates substantially affect their clock operation and attainable uncertainties[16,26,27,31,33]. Although the lifetime measurement studying hyperfine interaction in many-electron HCIs has already been reported[43], spectroscopic measurements of hyperfine-structure constants in many-electron HCIs have not proceeded.

Here, we study the hyperfine structures in the $4d^9 5s$ metastable states of Pd-like $^{127}I^{7+}$ using laser-induced fluorescence (LIF) spectroscopy. Historically, LIF spectroscopy of trapped HCIs free from systematic Doppler shifts was pioneered by Hosaka et al.[44]. They demonstrated a CW-laser-induced fluorescence spectroscopy of the electric-dipole (E1)-allowed transition $2s$-$2p_{3/2}$ of H-like ions in an electron beam ion trap (EBIT) plasma by monitoring the enhancement of the Lyman-α emission[45]. In the past decade, resonant laser spectroscopy (RLS) of forbidden transitions using a combination of pulsed laser and time-resolved fluorescence detection has investigated the simple doublet fine-structure splittings in Ar^{13+} (see ref. [46]) and Fe^{13+} (see ref. [47]) under a strong magnetic field without an electron beam. In this paper, we demonstrate time-resolved LIF spectroscopy of HCIs in an EBIT using E1-forbidden transitions both for laser excitation and fluorescence detection. High-resolution spectroscopy of the transition between highly excited metastable states is achieved with the aid of excitation processes in the EBIT plasma. A similar experimental scheme was proposed for $3d^9 4s$ in Ni-like HCIs[48]; however, this has not yet been demonstrated. It is worth emphasizing that we operate the EBIT with a low magnetic field condition to suppress the Zeeman splitting and employ the evaporative cooling technique for reduction of the Doppler line broadening, leading to clear observation of the hyperfine splitting.

Results

Concept of the plasma-assisted laser spectroscopy. In the present experiment, we prepare the $(4d^9_{5/2}5s)_{J=3}$ metastable state of $^{127}I^{7+}$ in an EBIT and irradiate the trapped HCI with a pulsed laser, as shown in Fig. 1a. Figure 1b shows the experimental scheme used with the level structure of $^{127}I^{7+}$. Due to the closed $4d^{10}$ shell structure in the ground state, the excitation energy to the first excited fine-structure level $(4d^9_{5/2}5s)_{J=3}$ is relatively high at ~47 eV. Although such high-energy states are generally de-excited in a short time, the lifetimes for every hyperfine level in $(4d^9_{5/2}5s)_{J=3}$ are longer than 10 s because their de-excitation processes are strongly forbidden, except for M3 and hyperfine-mixing E2 transitions. From the long-lived fine-structure level, the extreme ultraviolet (EUV) electric-quadrupole (E2) transition $((4d^9_{3/2}5s)_{J=2} \rightarrow (4d^{10})_{J=0})$ was induced by pulsed laser excitation via the M1 transition $((4d^9_{5/2}5s)_{J=3} \rightarrow (4d^9_{3/2}5s)_{J=2})$. Both the initial and excited levels in the laser excitation are metastable states without any E1 decay path; thus, the natural width of the transitions is estimated to be ~10^{-5} cm^{-1} (1 cm^{-1} = 2.99792×10^{10} Hz) from the theoretical 4 μs lifetime of the upper fine-structure level $(4d^9_{3/2}5s)_{J=2}$. The intrinsically narrow natural width of the laser transitions contributes to the high resolution in spectroscopic measurements, revealing the hyperfine structure.

The long-lived state $(4d^9_{5/2}5s)_{J=3}$ of $^{127}I^{7+}$ was continuously prepared through collisional and radiative processes in the EBIT plasma. Although increasing the number of trapped ions necessitates an enhanced electron density of the plasma, electron collisions must be suppressed to detect LIF emissions from the laser-excited fine-structure level with a lifetime in the order of microseconds. We controllably maintained the EBIT electron density below 10^{10} cm^{-3}, where the total collisional excitation and de-excitation rate out of the $(4d^9_{3/2}5s)_{J=2}$ level was approximately 10^3 s^{-1}(see ref. [49]). The production rate of $(4d^9_{5/2}5s)_{J=3}$ under an electron density of 10^{10} cm^{-3} was estimated to be ~160 s^{-1} from collisional-radiative modeling[49]. Thus, the excitation rate by the pulsed laser was operated at less than 1 s^{-1} to avoid depletion of the population in the initial state $(4d^9_{5/2}5s)_{J=3}$. This well-designed closed transition cycle, including the plasma processes, maintains the sequential LIF detection, suppressing the unintended population loss for the initial and excited levels in the laser excitation. We emphasize that the well-defined laboratory plasma and its control along with a deep understanding of the excitation and de-excitation dynamics through collisional-radiative modeling allow us the LIF detection, even though the ions are in plasma.
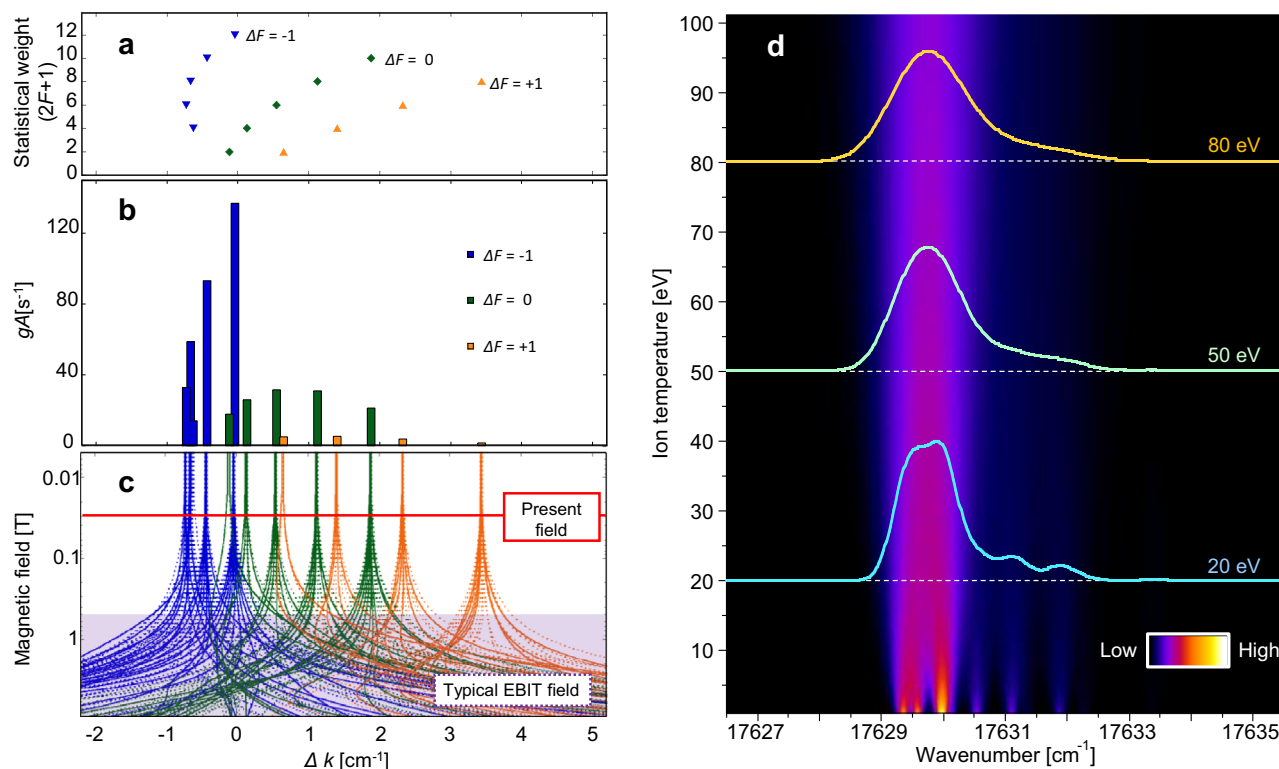
The hyperfine splitting for each fine-structure level is given by the magnetic-dipole hyperfine-structure constant A_{hfs}, the electric-quadrupole hyperfine-structure constant B_{hfs}, and the quantum numbers J, F, and I. A_{hfs} and B_{hfs} are relevant values to the atomic structure and the nuclear moments. The nuclear properties of ^{127}I, the only stable isotope of iodine, have been well investigated[50]: nuclear spin $I = 5/2$, nuclear magnetic moment $\mu_I = 2.81327(8)\mu_N$ and nuclear electric-quadrupole moment $Q_I = 0.689(15)$ b. We calculated the hyperfine-structure constants and splittings for $(4d^9_{5/2}5s)_{J=3}$ and $(4d^9_{3/2}5s)_{J=2}$ using the atomic calculation code GRASP2018[41] as shown in Fig. 1b. In general, a contracted electron orbital in HCIs enhances the hyperfine splitting. In addition, in the present atomic system, the 5s electron orbital in the HCI has a significant overlap with the nucleus, resulting in large hyperfine splitting. In fact, our theoretical calculation shows that the A_{hfs} constant for $(4d^9_{5/2}5s)_{J=3}$ in $^{127}I^{7+}$ is six times larger than that for $4d^9_{5/2}$ in $^{127}I^{8+}$, even though the binding energy is smaller.
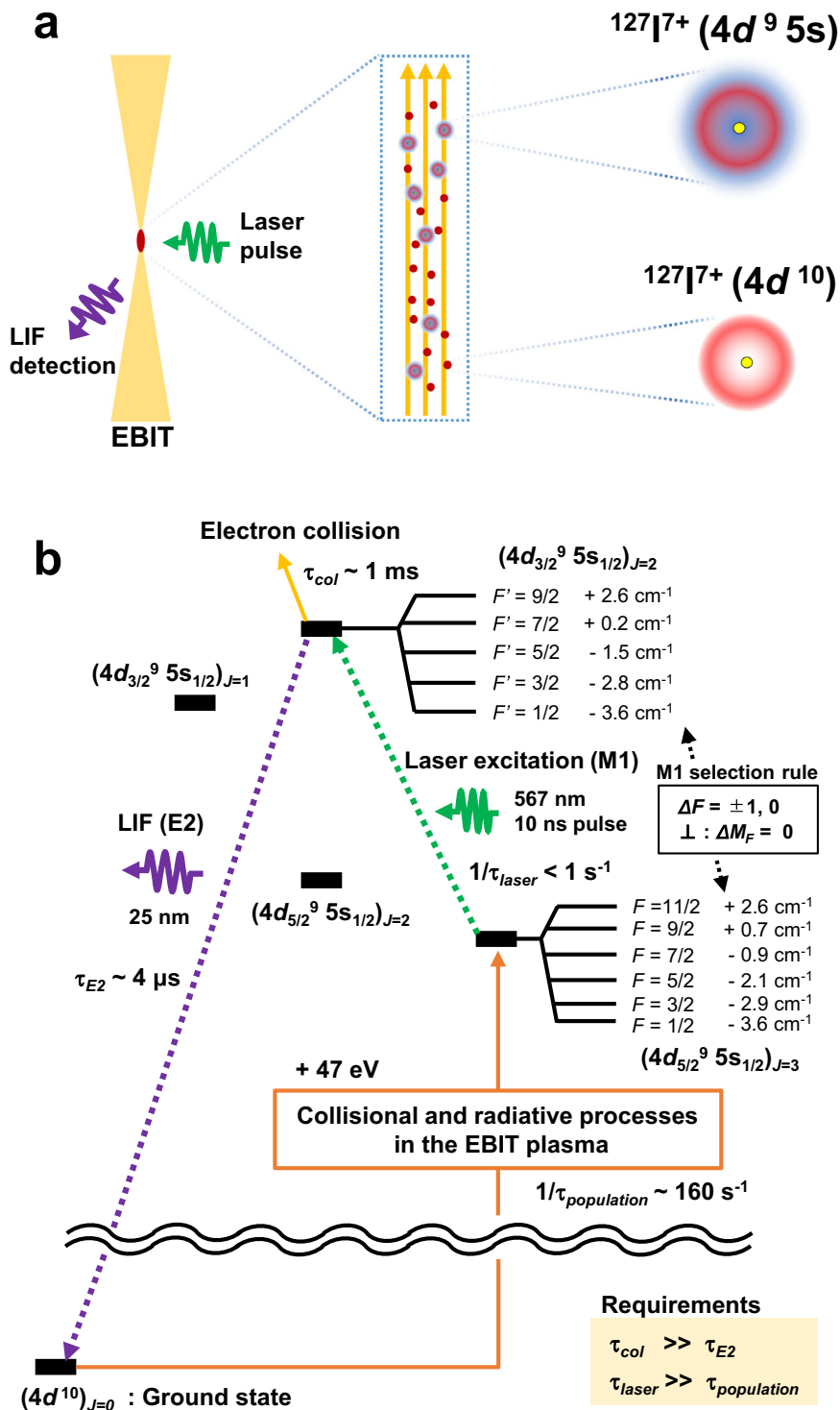
Fig. 1 Schematic diagram of the present laser spectroscopy. a Brief overview of the present laser-induced fluorescence (LIF) spectroscopy with the schematic trap region and ions. **b** Experimental scheme with the energy diagram of $^{127}I^{7+}$. The population rate of $(4d^9_{5/2}5s)_{J=3}$ ($1/\tau_{population}$) was estimated, using collisional-radiative modeling[49]. τ_{col}, τ_{E2}, and τ_{laser} are depopulation lifetimes by electron collision, electric-quadrupole ($E2$) radiative decay, and laser-induced magnetic-dipole ($M1$) excitation, respectively. An electron energy of 105 eV and a density of 10^{10} cm^{-3} are assumed in the collisional-radiative rates, corresponding to the present experimental condition. The energy structure and lifetime were calculated using GRASP2018[41].

Prediction of the spectral profile. The hyperfine structures split the laser transition into 14 components, considering the selection rules for $M1$ transitions ($\Delta F = \pm 1, 0$). Spectral simulations were performed to predict the features of the laser excitation spectrum, including hyperfine structures. Figure 2a shows the statistical weight of the initial state with the wavenumber deviation Δk corresponding to the difference from the original transition energy without the hyperfine structures. Figure 2b shows the spectral intensity gA, which is the sum of Einstein A coefficients of the $\Delta m_F = 0$ transitions for every magnetic sub-level. We also calculated the Zeeman splitting using the intermediate magnetic field treatment, as shown in Fig. 2c. Equations and atomic codes

Fig. 2 Theoretical predictions for the hyperfine-structure splitting in the laser excitation. a Statistical weights of the initial state $(4d^9_{5/2}5s)_{J=3}$. **b** Spectral intensity (gA). **c** Zeeman splitting. Solid and dotted lines show the $\Delta m_F = 0$ and $\Delta m_F = \pm 1$ transitions, respectively. The red line represents the present experimental condition. The typical magnetic field in an electron beam ion trap (EBIT) is shown by the purple shade. **d** Doppler broadening simulation. The transition energy was taken from the NIST database[55].

are summarized in "Methods". According to the simulation, the $M1$ transition lines are distributed over several cm^{-1}, and the spectral features under low magnetic field conditions have an asymmetric profile because of their specific quantum numbers and the intrinsic difference in the Racah coefficients between these transitions. At high magnetic fields above 0.5 T, such as that in a typical EBIT, magnetic sub-level-resolved transitions spread over a wide Δk range, which hinders the experimental assignment of hyperfine components. To overcome this difficulty, we employed the low magnetic field operation (0.03 T) of a compact electron beam ion trap (CoBIT)[51] at the University of Electro-Communications. Although this magnetic field is not classified as the weak-field limit, it is sufficiently low enough to suppress the Zeeman splitting below 0.05 cm^{-1}. The asymmetries of these splittings are less than 0.01 cm^{-1}. This quasi-Zeeman-free condition enables us to resolve the hyperfine structures.

In the present experiment, line broadening is expected to be dominated by the Doppler effect due to ion motion in the EBIT, since the Zeeman splitting, laser linewidth, and natural width of the transition are all less than 0.05 cm^{-1}. Figure 2d shows the spectral broadening simulation under the assumption of a Maxwellian distribution for the kinetic energies of the trapped ions in the EBIT[52]. In the low-temperature region, the width of each transition line becomes narrow, and the associated features originating from the $F = 7/2 \rightarrow F' = 7/2$ and $F = 9/2 \rightarrow F' = 9/2$ transitions appear around 17,631–17,632 cm^{-1}. The simulation shows that the ions should be cooled below 20 eV to characterize the hyperfine structures and determine the spectroscopic parameters.

Measurement of the laser-induced fluorescence. Figure 3a shows the present experimental setup. From CH$_3$I vapor, ^{127}I^{7+} ions were produced by an electron beam and stored in an electrostatic trap potential formed by the electron beam and three

successive cylindrical drift-tube (DT) electrodes[49]. To efficiently produce ^{127}I^{7+} ions, the electron beam energy (105 eV) and current (2 mA) were experimentally determined by monitoring the emission intensity of the $E2$ transition $(4d^9_{3/2}5s)_{J=2} \rightarrow (4d^{10})_{J=0}$[49]. To excite the $M1$ transitions, we used a wavelength-tunable dye laser (Sirah Cobra-Stretch with the dual 3000 lines/mm grating option, Exciton Rhodamine 6G/ Ethanol dye solution, 567 nm) pumped by the second harmonic of an Nd:YAG nanosecond-pulsed laser (Cutting Edge Optics Gigashot, 10 ns) with a 100 Hz repetition rate. The wavelength of the laser was monitored using a high-precision wavemeter (High Finesse, WS-6-600). The laser pulse energy was tuned and maintained at ~7 mJ/ pulse by the combination of a $\lambda/2$ wave plate and polarizer. The polarization of the laser was perpendicular to the magnetic field so that only the $\Delta m_F = 0$ transitions were excited. LIF was monitored with a time-resolving extreme ultraviolet (EUV) spectrometer consisting of an aberration-corrected concave grating (Hitachi 001-0660) and a position-sensitive detector (PSD, Quantar Technology Inc., model 3391)[53]. A typical ^{127}I^{7+} emission spectrum obtained with the EUV spectrometer is shown in Fig. 3b. Owing to the large difference in wavelength, the LIF signal can be readily distinguished from the laser-scattering noise. The prominent line at 49 eV is the targeted $E2$ transition $((4d^9_{3/2}5s)_{J=2} \rightarrow (4d^{10})_{J=0})$, which was used to detect laser excitation. To distinguish the LIF signal from the continuous emission induced by collisional and radiative processes in the plasma, the time spectrum of the $E2$ transition was recorded with a Multi-Channel-Scaler (MCS) as shown in Fig. 3c. The observed lifetime of the LIF signal was ~4 μs, which agrees with our theoretical calculation.

LIF spectrum and its analysis. Figure 4 shows the laser wavelength spectrum of the LIF signal. It took a few hours to
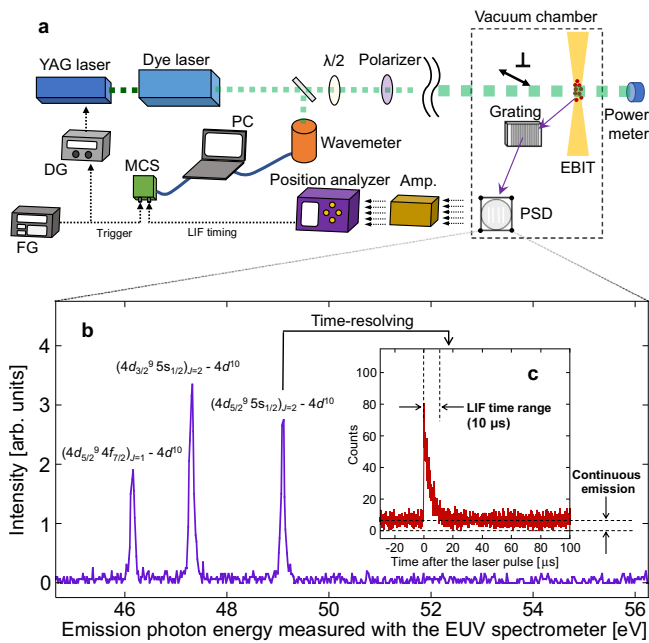
Fig. 3 Overview of the LIF detection setup. a Schematic of the experimental setup consisting of the electron beam ion trap (EBIT) with a time-resolved laser-induced fluorescence (LIF) detection system. FG, DG, MCS, and PSD represent a Function Generator, Delay Generator, Multi-Channel-Scaler, and Position-Sensitive detector, respectively. **b** Typical EUV emission spectrum. **c** Time-resolved signal for the laser-induced $E2$ transition fluorescence.

Fig. 4 Experimental LIF spectrum. The fitting result (black line) is shown with separated profiles (blue, green, and orange lines) for every transition. The error bar for each experimental data point (red diamond) represents the statistical error.

accumulate LIF counts at each wavelength. To compensate for possible fluctuation in the number of stored ions, the LIF counts were normalized by continuous $E2$ counts, which are regarded to be proportional to the ion number. The vertical axis in Fig. 4 represents the ratio of LIF signal counts within 10 μs after laser irradiation to the total counts, including the continuous emission within the interval of laser irradiation (10 ms). The background level due to continuous plasma emission in the ratio was directly determined to be 0.001 from the time range ratio (10 μs/10 ms). In a preliminary scan, a broad main structure at 17,633–17,634 cm^{-1} and associated structures at 17,634–17,636 cm^{-1} were observed. We considered that the associated structures were important for understanding the origin of the spectral features. Therefore, a finer wavelength scan of this region was performed to obtain higher statistics, as shown in Fig. 4. In the fine scan, all DT electrodes were set to ground potential to suppress the Doppler line broadening. While the axial potential formed by the electron beam still enables the storage of ^{127}I^{7+} ions, the resulting shallow axial potential allows for evaporative cooling, yielding a reduction in the spectral linewidth[52,54]. Comparing results to the spectral simulation, we conclude that the main and associated features are primarily composed of $\Delta F = -1$ and 0 transitions, respectively.

To determine the hyperfine-structure constants, the observed spectrum was fitted with a model function incorporating all hyperfine-resolved transitions with the same Doppler width k_D. The model function is described in "Methods". The center of the transition energy for each line is determined by the original transition energy k_0 for the fine-structure transition and the hyperfine-structure constants for each of the initial and excited fine-structure levels. The relative line intensity for each transition was defined by the simulation intensity in Fig. 2b. Consequently, the seven parameters A_{hfs}, B_{hfs}, A'_{hfs}, B'_{hfs}, k_0, k_D, and total spectral
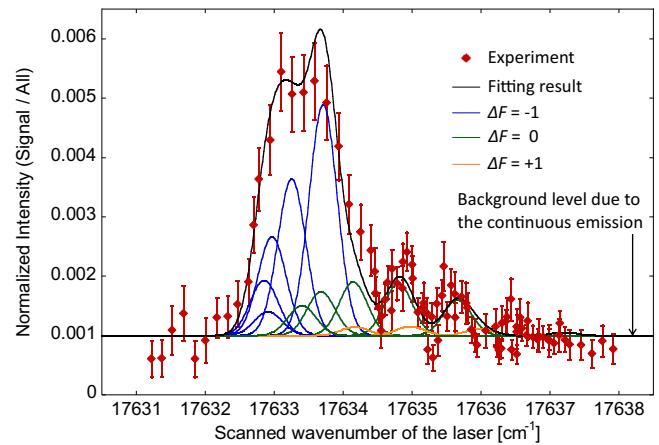
intensity I_0 were determined in the fitting procedure, where the primed quantities refer to the excited fine-structure level. Note that theoretically calculated Einstein A coefficients were used to determine the simulated intensities. The intensity model mainly depends on the Racah coefficients, whereas the actual intensity is slightly different because of the hyperfine mixing with other fine-structure levels. We theoretically evaluated the hyperfine-mixing effect on the transition intensities and found that this contribution is less than 0.05 s^{-1} for every Einstein A coefficient. This uncertainty in the model function affects the determination of the experimental values by less than 1 % of the experimental uncertainty and is thus considered insignificant. The statistical population in the intensity model may also be disturbed by the lifetime difference between hyperfine levels[43]. However, in the case of ^{127}I^{7+}, it is not necessary to consider such possibilities because the radiative decay rates are at least 10^3 times longer than the collisional-radiative rate supplying the population to the metastable fine-structure level; hence, the populations are not quenched by spontaneous decay to the ground state. Thus, we consider the intensity model used here to be reasonable for determining the constants. The fitted profiles for each hyperfine component and their convolution are shown in Fig. 4. The obtained parameters are listed in Table 1 along with the theoretical values calculated by the GRASP code taking the Breit and quantum electrodynamic (QED) effects into account. The reduced-chi-square in the fitting was 1.1. From the laser wavelength stability during the measurement, the systematical errors for the hyperfine-structure constants were estimated to be 0.3 GHz. The systematic error of k_0 is 0.03 cm^{-1} taking the absolute accuracy of the wavemeter into account. The resulting k_D is 0.46 (±0.04) cm^{-1} corresponding to an ion temperature of 15 (±2) eV under the assumption that Doppler broadening dominates in the spectral linewidth. The shallow trapping potential formed by the zero DT voltage and the thin electron density with a low magnetic field enabled the trapped ions to be evaporatively cooled down to temperatures similar to those found in forced evaporative cooling by turning off the electron beam[46]. The narrow Doppler width realized in the present measurement is essentially important for resolving the hyperfine splitting.

Because the nuclear spin and moments of ^{127}I are well-known[50], the experimentally obtained hyperfine-structure constants are used to validate the theoretical calculation of the electron orbital for each fine-structure level. Experimental results obtained here show reasonable agreement with theoretical values, considering the

Table 1 Summary of the experimental and theoretical values for $(4d^9_{5/2}5s)_{J=3}$ and $(4d^9_{3/2}5s)_{J=2}$ in $^{127}I^{7+}$.

	Experiment	Theory	MCDF	Breit	QED
A_{hfs} [GHz]	10.3 ($\pm$ 0.3$_{stat}$ $\pm$ 0.3$_{sys}$)	10.39 ($\pm$ 0.05)	10.41	-1.7×10^{-2}	$+3.3 \times 10^{-3}$
B_{hfs} [GHz]	2.9 ($\pm$ 1.8$_{stat}$ $\pm$ 0.3$_{sys}$)	2.32 ($\pm$ 0.02)	2.37	-4.3×10^{-2}	$+4.0 \times 10^{-4}$
A'_{hfs} [GHz]	15.8 ($\pm$ 0. 3$_{stat}$ $\pm$ 0.3$_{sys}$)	15.33 ($\pm$ 0.03)	15.45	-1.2×10^{-1}	$+7.5 \times 10^{-3}$
B'_{hfs} [GHz]	1.5 ($\pm$ 1.4$_{stat}$ $\pm$ 0.3$_{sys}$)	2.02 ($\pm$ 0.01)	2.05	-2.8×10^{-2}	$+3.0 \times 10^{-4}$
k_0 [cm^{-1}]	17633.67 ($\pm$ 0.02$_{stat}$ $\pm$ 0.03$_{sys}$)	17616 ($\pm$ 22)	18016	-418	$+18$

The theoretical results are obtained by Multi-configuration Dirac-Fock calculations combined with the relativistic configuration-interaction (RCI) approach, as described in "Methods". The RCI corrections of the generalized Breit interaction and the QED effects (self-energy and vacuum polarization) are separately shown.

uncertainties. The transition energy k_0 obtained by the experiment agrees with the theoretical calculation within ~0.1%. The Breit interaction shifts the transition energy by 2%, which is important to reproduce the experimental result. The energy of each fine-structure level has been compiled in the NIST database[55] from several experimental results using passive spectroscopy, and the uncertainty was evaluated to be 100 cm^{-1}. In the present study, we clearly demonstrate that our active spectroscopic approach succeeded in directly measuring the transition energy and greatly reducing its uncertainty. This clarified the importance of the relativistic configuration-interaction (RCI) correction for the Breit interaction.

Discussion

We have demonstrated laser spectroscopy of forbidden transitions between metastable states of HCIs stored in an EBIT by employing Pd-like $^{127}I^{7+}$. The laser excitation spectrum of the HCIs in a quasi-Zeeman-free low magnetic field revealed distinct hyperfine structures, which provided evidence for the enhancement of the hyperfine interaction via a contracted electron cloud with a $5s$ valence electron. The resulting hyperfine-structure constants of highly charged ions with a well-known nucleus provide a benchmark for atomic orbital calculations with relativistic many-electron correlations, allowing for discussion of the electron cloud in the vicinity of the nucleus for each fine-structure level. Even though the transition observed in this study is not a proposed HCI clock candidate, the building of a benchmark to understand hyperfine structures in many-electron HCIs makes a significant step toward developing such clocks, considering especially that the currently most promising clock candidates with a $5s$-$4f$ level crossing[15–18,20,23–28,32] are intrinsically accompanied by a similar characteristic electron configuration having a single $5s$ electron. The established benchmarks would serve as a reference to enhance the understanding of the hyperfine interaction in many-electron HCIs.

The present hyperfine-structure-resolved laser spectroscopy offers future possibilities for experimental studies in nuclear physics using HCIs, such as a broad investigation of unknown nuclear spins and moments and hyperfine anomalies with a specialized EBIT for highly charged radionuclide ions[56]. Recently, high-precision atomic orbital calculations have been extensively developed to investigate nuclear properties from hyperfine-structure constants[57–61]. While this approach had the privilege for particular nuclei with optically accessible transitions at low valence ions, the extension of the target to HCIs enables the selection of an atomic-level structure by changing the charge state. In addition, an ns-valence state enhancing its hyperfine interaction can be arbitrarily selected, in contrast to neutral atoms or singly charged ions whose electron configurations are fixed. We consider that the present LIF scheme has the potential to be a versatile method for investigating heavy nuclear properties because it can be directly applied to the three transitions in Pd-like ions and Ni-like ions, as follows. Pd-like ions have an additional excitation pathway from the long-lived $(4d^9_{5/2}5s)_{J=3}$ state to the $(4d^9_{5/2}5s)_{J=2}$ excited fine-structure level via an $M1$-allowed transition. Ni-like ions have a similar

energy level system with the $3d^{10}$ closed ground state. Therefore, the investigation of the $(3d^9_{5/2}4s)_{J=3} \rightarrow (3d^9_{3/2}4s)_{J=2}$ and $(3d^9_{5/2}4s)_{J=3} \rightarrow (3d^9_{5/2}4s)_{J=2}$ transitions with the present laser spectroscopy scheme is also possible. The laser spectroscopy of $(3d^9_{5/2}4s)_{J=3} \rightarrow (3d^9_{5/2}4s)_{J=2}$ transitions in Ni-like ions has already been proposed, and their transition wavelengths have been systematically investigated by theoretical calculations[48]. Here, we follow the systematic study to discuss the versatility of the present laser spectroscopy. Figure 5 shows the atomic number dependence of the transition energies theoretically calculated by the FAC[62], along with optical $E1$ transition energies of Ag-like ions for comparison. In the $Z > 60$ region, Pd-like ions are not shown because they are not suitable for the present laser spectroscopy since the $(4d^9_{5/2}5s)_{J=3}$ level is not metastable due to the $4d^95s$-$4d^94f$ level crossing[63]. In contrast to the typical electronic $E1$ transitions (e. g., $5s$-$5p_{1/2}$ in Ag-like ions), the present $M1$ transitions with a number of inner-shell electrons show a gradual increase in the transition energy with increasing atomic number. As a result, in most regions where $Z > 30$, transitions in either Pd- or Ni-like ions are available for laser excitation.

The present demonstration achieved precise determination of the transition energy with an uncertainty of $\Delta k/k_0 \simeq 3 \times 10^{-6}$ for the $M1$ transition, which is inaccessible by emission spectroscopy due to the rapid $E2$ decay path from the upper fine-structure level. From a technical perspective, we have succeeded in extending precision spectroscopy for trapped HCIs from spontaneously emitted transitions to include non-luminescent transitions, providing a wider variety of spectroscopic targets. This offers various opportunities, including the investigation of HCI clock candidates. Prospects of the HCI atomic clock have also spurred developments in HCI laser spectroscopy with part-per-million uncertainties. Several laser spectroscopic methods for forbidden transitions of trapped HCIs free from systematic Doppler shifts have been reported[46,64]. These demonstrations employed a simple fine-structure transition $^2P_{1/2}$-$^2P_{3/2}$ in the doublet ground term of Ar^{13+}, whose transition energy is precisely known from direct wavelength measurements using passive spectroscopy[65,66], leading to recent quantum logic spectroscopy[36,37]. However, many potential candidates for the HCI atomic clock are not directly accessible using such passive spectroscopy because they possess complicated level structures with hyperfine splitting, and their clock transitions do not emit in plasmas owing to their long lifetime. Therefore, the extension of laser spectroscopy of HCIs to complex systems is an important challenge to overcome. The present scheme can be applied to investigate the repump transitions and measure the hyperfine-structure constants of a clock state, which are otherwise not accessible using passive spectroscopic methods.

Finally, we discuss the possibilities of other applications using the present spectroscopic technique. The time-resolved LIF detection technique can be applied to hyperfine-level-selective lifetime measurements without cascade contributions from higher levels, leading to deeper investigations of hyperfine interaction[43],
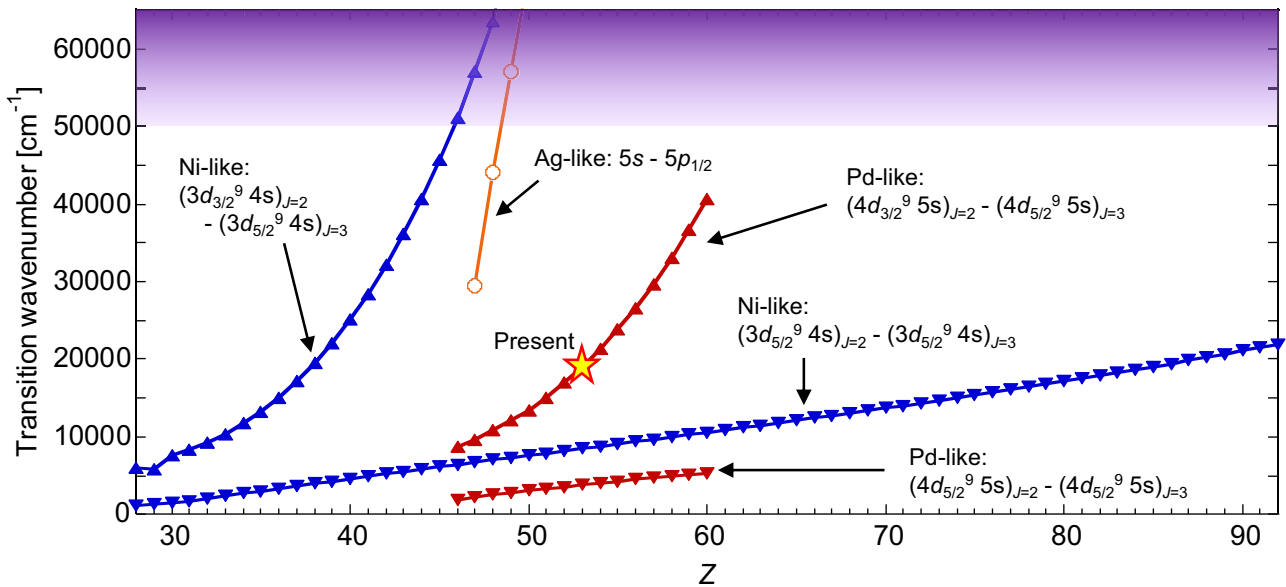
Fig. 5 Potential of the present laser spectroscopy for studying heavy nuclei. Atomic number (Z) dependence of the theoretical transition energies in Pd-like (red) and Ni-like (blue) ions, along with the transition energies of the $E1$ transition $5s$–$5p_{1/2}$ in Ag-like ions (orange) for comparison. The present transition $(4d_{3/2}^9 5s)_{J=2}$ - $(4d_{5/2}^9 5s)_{J=3}$ in $^{127}I^{7+}$ is highlighted by the star symbol. The purple-shaded region indicates wavelength ranges where it is generally difficult for lasers to reach (<200 nm).

including hyperfine-induced-interference effects[67] which have not yet been experimentally observed. The demonstration of laser spectroscopy of forbidden transitions for HCIs in a laboratory plasma is expected to trigger the development of active sensing to investigate plasma conditions such as the plasma ion temperature and magnetic field, contributing to plasma diagnostics.

Methods

Theoretical transition energy. The transition energy between the fine-structure levels in $4d^9 5s$ is obtained in the framework of multi-configuration Dirac-Fock (MCDF) calculations, combined with the relativistic configuration-interaction (RCI) approach, using the atomic-structure calculation code package GRASP2018[41]. First, MCDF calculations were performed with an active space of single- and double-electron excitation from the $4s$, $4p$, and $4d$ orbitals up to $8g$. Each nl orbital ($n = 5$–8, $l = s, p, d, f, g$) is added individually, with each outer orbital optimized while keeping all inner orbitals fixed. Furthermore, to account for core–core and core–valence correlations with the inner orbitals, excitations from the $3l$ ($l = s, p, d$) orbitals were also included. This active space treatment led to 3,300,000 jj-coupled configurations. Moreover, corrections from the Breit interaction, that is transverse photon interaction in the low-frequency limit, and QED corrections separating the self-energy and vacuum polarization corrections, are included in the RCI calculation.

Theoretical hyperfine-structure constants. Using the GRASP2018 code, we calculated the magnetic-dipole hyperfine-structure constant A_{hfs} and electric-quadrupole hyperfine-structure constant B_{hfs} for each fine-structure level $((4d_{5/2}^9 5s)_{J=3}$ and $(4d_{3/2}^9 5s)_{J=2})$. For the input values, the nuclear magnetic moment μ_I and nuclear electric-quadrupole moment Q_I were taken from ref. [50]. GRASP2018 also provides hyperfine-structure splitting calculations taking hyperfine mixing with other fine-structure levels into account. We compared two calculation cases, i.e., with and without considering shifts due to hyperfine mixing. It was found that the resulting shift in energy for each hyperfine level would be unobservable in the experiment. Each correction for the hyperfine-structure constants was also evaluated using the same procedure as for the transition energy calculation.

Estimation of uncertainties for the theoretical values. There are several origins of uncertainties in the theoretically calculated values due to various corrections. The uncertainties in the transition energy were estimated as follows: The present MCDF-CI calculations involve valence–valence (VV), core–valence (CV), and core–core (CC) correlations. They are considered by including configurations generated from all single- and double-excitations from the $3s$, $3p$, $3d$, $4s$, $4p$, $4d$, and $5s$ orbitals to the active spaces (AS) of virtual orbitals. Here we define four virtual orbital sets as follows: AS1 = {$5p$, $5d$, $5f$, $5g$}, AS2 = AS1 + {$6s$, $6p$, $6d$, $6f$, $6g$, $6h$}, AS3 = AS2 + {$7s$, $7p$, $7d$, $7f$, $7g$, $7h$}, and AS4 = AS3 + {$8s$, $8p$, $8d$, $8f$, $8g$, $8h$}. We estimated the convergence with the size of the basis set by taking the difference

between the transition energies calculated in the AS3 and AS4 stages ($\simeq 22$ cm^{-1}). The calculated transition energies are summarized in Supplementary Table I. The detail of the corrections in the full active space set (AS4) calculation result is shown in Supplementary Table II. We adopted this value for the uncertainty in the electron correlation calculation because additional correlations were not expected to exceed this convergence value even when considering more virtual orbitals. Another possible source of uncertainty is related to the calculated contribution from the Breit interaction. The corresponding correction value was perturbatively computed in the RCI calculation through the exchange of a single transverse photon in the low-frequency limit[41,68]. Comparing the Breit contributions obtained from the perturbative approach to calculations in which the Breit term is included in a variational SCF process allows us to estimate the uncertainty due to the perturbative approach[69,70]. Previous studies have found that the magnitude of this effect is less than 0.3% in the Ni-like case (among others)[69,70] and that it is significantly reduced when the active space is expanded. Here, we assume the maximum error owing to the perturbative treatment and adopt a 0.5% uncertainty related to the Breit correction. The resulting uncertainty is 2 cm^{-1}. The QED contributions were smaller than the uncertainties related to correlation effects. Thus, the resulting uncertainty associated with these terms was negligible. The uncertainty in the Dirac-Fock term is caused by the uncertainty in the root-mean-square of the nuclear radius, which is insignificant for ^{127}I ($\simeq 0.008$ fm[71]). The total uncertainty was calculated by applying the error propagation rule (quadratic summation) to individual sources of uncertainty. This yielded an uncertainty in the theoretical transition energy of 22 cm^{-1}. This uncertainty is strongly dominated by the electron correlation. We also estimated the uncertainty for each A_{hfs} and B_{hfs} constant by employing the same procedure adopted for the transition energy.

Simulation of the Zeeman splitting. The Zeeman splitting for each hyperfine level was calculated using the HFSZEEMAN95 package[72,73], which is based on inputs from GRASP2018[41]. This calculation employs an accurate treatment of the intermediate field regime; therefore, the calculated splittings are reliable for a wide range of magnetic fields. Figure 2c shows the differences in the Zeeman splitting between the initial and excited levels of the laser transition.

Simulation of the transition intensities. The hyperfine-structure-resolved Einstein A coefficients were obtained by the summation of the Einstein A coefficients for every $\Delta m_F = 0$ transition at each initial hyperfine-structure level. The transition rate for an $M1$ transition between magnetic hyperfine-structure sub-levels $\Gamma' m_F'$ and Γm_F is given by

$$A(\Gamma' m_F' \rightarrow \Gamma m_F) = \frac{2.69735 \times 10^{13}}{\lambda^3} \sum_q |\langle \Gamma m_F | M_q^{(1)} | \Gamma' m_F' \rangle|^2, \quad (1)$$

where $M^{(1)}$ is the magnetic-dipole operator, and λ is the transition wavelength (in Å). Using the wavefunction expansion of the magnetic hyperfine substates,

$$|\Gamma m_F\rangle = \sum_{\gamma, J, F} d_{\gamma, J, F} |\gamma I J F m_F\rangle \quad (2)$$

together with the Wigner–Eckart theorem (the dipole operator only acts on the electronic space, so we may decouple the nuclear and electronic parts in the reduced matrix element), Eq. (1) can be re-written as[73]

$$A(\Gamma' m_F' \rightarrow \Gamma m_F) =$$

$$\frac{2.69735 \times 10^{13}}{\lambda^3} \sum_q |\sum_{\gamma JF} \sum_{\gamma' J' F'} d_{\gamma JF} d_{\gamma' J' F'}$$

$$\sqrt{(2F'+1)(2F+1)}(-1)^{F-m_F}$$

$$\begin{pmatrix} F & 1 & F' \\ -m_F & q & m_F' \end{pmatrix}(-1)^{I+J'+F+1} \tag{3}$$

$$\begin{Bmatrix} J & F & I \\ F' & J' & 1 \end{Bmatrix} \langle \gamma J || M^{(1)} || \gamma' J' \rangle|^2.$$

Here, $d_{\gamma JF}$ are the expansion coefficients, and $\langle \gamma J || M^{(1)} || \gamma' J' \rangle$ is the reduced transition matrix element between the fine-structure levels. The A coefficients for all $M1$ transitions were calculated using the HFSZEEMAN95 package[72,73]. Finally, we sum the Einstein A coefficients for the $\Delta m_F = 0$ transitions of every m_F sub-level and obtained the transition intensities gA of the $M1$ transitions, as shown in Fig. 2b.

Fitting model. We determined the hyperfine-structure constants A_{hfs}, B_{hfs}, A'_{hfs}, B'_{hfs} and the fine-structure transition wavenumber k_0 using the following model equation to fit experimental data:

$$f(k) = I_0 \sum_{|F'-F| \leq 1} gA_{F'F} \exp\left(\frac{4\ln 2(k-(k_0+k_{F'F}))}{k_D^2}\right). \tag{4}$$

Here, it is assumed that each line profile is defined by a Gaussian function with the same linewidth because the hyperfine splitting energies are significantly smaller than the fine-structure transition energy. k_D represents the full-width at half maximum (FWHM) of the transition line profiles. For $gA_{F'F}$, we employed theoretically calculated results for the relative transition intensities, as described in the previous section. k_0 is the original transition energy between the fine-structure levels ($(4d^9_{5/2}5s)_{J=3} \rightarrow (4d^9_{3/2}5s)_{J=2}$). $k_{F'F}$ is the hyperfine-structure shift for each transition given by

$$k_{F'F} = k_{F'} - k_F. \tag{5}$$

k'_F and k_F are hyperfine-structure shifts from the original level for $(4d^9_{3/2}5s)_{J=2}$ and $(4d^9_{5/2}5s)_{J=3}$, respectively. The hyperfine splitting at each fine-structure level is given by

$$k_{F'} = \frac{1}{2}A'_{hfs}C' + B'_{hfs}\frac{\frac{3}{4}C'(C'+1)-I(I+1)J'(J'+1)}{2I(2I-1)J'(2J'-1)} \tag{6}$$

and

$$k_F = \frac{1}{2}A_{hfs}C + B_{hfs}\frac{\frac{3}{4}C(C+1)-I(I+1)J(J+1)}{2I(2I-1)J(2J-1)}. \tag{7}$$

Here, C' and C are given by:

$$C' = F'(F'+1) - J'(J'+1) - I(I+1) \tag{8}$$

and

$$C = F(F+1) - J(J+1) - I(I+1). \tag{9}$$

Under the assumption of a Maxwellian distribution, the equation for the ion temperature and spectral linewidth is given by:

$$T = \frac{Mc^2}{8k_B \ln 2}\left(\frac{k_D}{k_0}\right)^2, \tag{10}$$

where M, c, and k_B are the particle mass, speed of light, and Boltzmann constant, respectively. Equation (10) can be re-written as:

$$k_D = \sqrt{\frac{8Tk_B \ln 2}{M}}\frac{k_0}{c}. \tag{11}$$

Equations (11) and (4) provide theoretical spectra.

Data availability
The data that support the findings of this study are available from the corresponding author upon reasonable request.

Code availability
The FAC is available at https://www-amdis.iaea.org/FAC/, the GRASP2018 code at https://www-amdis.iaea.org/GRASP2K/, and the HFSZEEMAN95 code at https://doi.org/10.17632/rv2vycs7pg.1.

References
1. Campbell, P., Moore, I. D. & Pearson, M. R. Laser spectroscopy for nuclear structure physics. *Prog. Part. Nucl. Phys.* **86**, 127 (2016).
2. Klaft, I. et al. Precision laser spectroscopy of the ground state hyperfine splitting of hydrogenlike ^{209}Bi^{82+}. *Phys. Rev. Lett.* **73**, 2425 (1994).
3. Seelig, P. et al. Ground state hyperfine splitting of hydrogenlike ^{207}Pb^{81+} by laser excitation of a bunched ion beam in the GSI experimental storage ring. *Phys. Rev. Lett.* **81**, 4824 (1998).
4. Crespo López-Urrutia, J. R., Beiersdorfer, P., Savin, D. W. & Widmann, K. Direct observation of the spontaneous emission of the hyperfine transition F=4 to F=3 in ground state hydrogenlike ^{165}Ho^{66+} in an electron beam ion trap. *Phys. Rev. Lett.* **77**, 826 (1996).
5. Crespo López-Urrutia, J. R. et al. Nuclear magnetization distribution radii determined by hyperfine transitions in the 1s level of H-like ions ^{185}Re^{74+} and ^{187}Re^{74+}. *Phys. Rev. A* **57**, 879 (1998).
6. Beiersdorfer, P. et al. Hyperfine structure of hydrogenlike thallium isotopes. *Phys. Rev. A* **64**, 032506 (2001).
7. Ullmann, J. et al. High precision hyperfine measurements in bismuth challenge bound-state strong-field QED. *Nat. Commun.* **8**, 15484 (2017).
8. Beiersdorfer, P., Osterheld, A. L., Scofield, J. H., Crespo López-Urrutia, J. & Widmann, K. Measurement of QED and hyperfine splitting in the 2s$_{1/2}$-2p$_{3/2}$ X-ray transition in Li-like ^{209}Bi^{80+}. *Phys. Rev. Lett.* **80**, 3022 (1998).
9. Beiersdorfer, P. et al. Hyperfine splitting of the 2s$_{1/2}$ and 2p$_{1/2}$ levels in Li- and Be-like ions of $_{59}$^{141}Pr. *Phys. Rev. Lett.* **112**, 233003 (2014).
10. Myers, E. G. et al. Laser-induced M1 resonance spectroscopy of the 1s2p ^{3}P$_1$ - ^{3}P$_2$ fine structure of ^{19}F^{7+}. *Phys. Rev. Lett.* **47**, 87 (1981).
11. Myers, E. G. et al. Measurement of the 1s2s^{1}S-1s2p^{3}P$_1$ interval in heliumlike nitrogen. *Phys. Rev. Lett.* **75**, 3637 (1994).
12. Myers, E. G., Howie, D. J. H., Thompson, J. K. & Silver, J. D. Hyperfine-induced 1s2s ^{1}S$_0$-1s2p ^{3}P$_0$ transition and fine-structure measurement in heliumlike nitrogen. *Phys. Rev. Lett.* **76**, 4899 (1996).
13. Thompson, J. K., Howie, D. J. H. & Myers, E. G. Measurements of the 1s2s^{1}S$_0$-1s2p^{3}P$_{1,0}$ transitions in heliumlike nitrogen. *Phys. Rev. A* **57**, 180 (1998).
14. Myers, E. G. et al. Precision measurement of the 1s2p^{3}P$_2$-^{3}P$_1$ fine structure interval in heliumlike fluorine. *Phys. Rev. Lett.* **82**, 4200 (1999).
15. Kozlov, M. G., Safronova, M. S., Crespo López-Urrutia, J. R. & Schmidt, P. O. Highly charged ions: optical clocks and applications in fundamental physics. *Rev. Mod. Phys.* **90**, 045005 (2018).
16. Berengut, J. C., Dzuba, V. A. & Flambaum, V. V. Enhanced laboratory sensitivity to variation of the fine-structure constant using highly charged ions. *Phys. Rev. Lett.* **105**, 120801 (2010).
17. Berengut, J. C., Dzuba, V. A., Flambaum, V. V. & Ong, A. Electron-hole transitions in multiply charged ions for precision laser spectroscopy and searching for variations in α. *Phys. Rev. Lett.* **106**, 210802 (2011).
18. Berengut, J. C., Dzuba, V. A., Flambaum, V. V. & Ong, A. Highly charged ions with E1, M1, and E2 transitions within laser range. *Phys. Rev. A* **86**, 022517 (2012).
19. Berengut, J. C., Dzuba, V. A., Flambaum, V. V. & Ong, A. Optical transitions in highly charged californium ions with high sensitivity to variation of the fine-structure constant. *Phys. Rev. Lett.* **109**, 070802 (2012).
20. Dzuba, V. A., Derevianko, A. & Flambaum, V. V. Ion clock and search for the variation of the fine-structure constant using optical transitions in Nd^{13+} and Sm^{15+}. *Phys. Rev. A* **86**, 054502 (2012).
21. Derevianko, A., Dzuba, V. A. & Flambaum, V. V. Highly charged ions as a basis of optical atomic clockwork of exceptional accuracy. *Phys. Rev. Lett.* **109**, 180801 (2012).
22. Yudin, V. I., Taichenachev, A. V. & Derevianko, A. Magnetic-dipole transitions in highly charged ions as a basis of ultraprecise optical clocks. *Phys. Rev. Lett.* **113**, 233003 (2014).
23. Safronova, M. S. et al. Highly charged ions for atomic clocks, quantum information, and search for α variation. *Phys. Rev. Lett.* **113**, 030801 (2014).
24. Safronova, M. S. et al. Highly charged Ag-like and In-like ions for the development of atomic clocks and the search for α variation. *Phys. Rev. A* **90**, 042513 (2014).
25. Safronova, M. S. et al. Atomic properties of Cd-like and Sn-like ions for the development of frequency standards and search for the variation of the fine-structure constant. *Phys. Rev. A* **90**, 052509 (2014).
26. Dzuba, V. A., Flambaum, V. V. & Katori, H. Optical clock sensitive to variations of the fine-structure constant based on the Ho^{14+} ion. *Phys. Rev. A* **91**, 022119 (2015).

27. Dzuba, V. A. & Flambaum, V. V. Hyperfine-induced electric dipole contributions to the electric octupole and magnetic quadrupole atomic clock transitions. *Phys. Rev. A* **93**, 052517 (2016).

28. Nandy, D. K. & Sahoo, B. K. Highly charged W^{13+}, Ir^{16+}, and Pt^{17+} ions as promising optical clock candidates for probing variations of the fine-structure constant. *Phys. Rev. A* **94**, 032504 (2016).

29. Cheung, C. et al. Accurate prediction of clock transitions in a highly charged ion with complex electronic structure. *Phys. Rev. Lett.* **124**, 163001 (2020).

30. Beloy, K., Dzuba, V. A. & Brewer, S. M. Quadruply ionized barium as a candidate for a high-accuracy optical clock. *Phys. Rev. Lett.* **125**, 173002 (2020).

31. Yu, Yan-mei & Sahoo, B. K. Investigating ground-state fine-structure properties to explore suitability of boronlike S^{11+}-K^{14+} and galliumlike Nb^{10+}-Ru^{13+} ions as possible atomic clocks. *Phys. Rev. A* **99**, 022513 (2019).

32. Windberger, A. et al. Identification of the predicted 5s-4f level crossing optical lines with applications to metrology and searches for the variation of fundamental constants. *Phys. Rev. Lett.* **114**, 150801 (2015).

33. Bekker, H. et al. Detection of the 5p-4f orbital crossing and its optical clock transition in Pr^{9+}. *Nat. Commun.* **10**, 5651 (2019).

34. Kimura, N. et al. Direct determination of the energy of the first excited fine-structure level in Ba^{6+}. *Phys. Rev. A* **100**, 052508 (2019).

35. Liang, S.-Y. et al. Probing multiple electric-dipole-forbidden optical transitions in highly charged nickel ions. *Phys. Rev. A* **103**, 022804 (2021).

36. Micke, P. et al. Coherent laser spectroscopy of highly charged ions using quantum logic. *Nature* **578**, 60 (2020).

37. King, S. A. et al. An optical atomic clock based on a highly charged ion. *Nature* **611**, 43 (2022).

38. Dzuba, V. A., Flambaum, V. V. & Sushkov, O. P. Relativistic many-body calculations of the hyperfine-structure intervals in caesium and francium atoms. *J. Phys. B: At. Mol. Phys.* **17**, 1953 (1984).

39. Jönsson, P. & Fischer, C. F. Large-scale multiconfiguration Hartree-Fock calculations of hyperfine-interaction constants for low-lying states in beryllium, boron, and carbon. *Phys. Rev. A* **48**, 4113 (1993).

40. Fischer, C. F. & Jönsson, P. MCHF calculations for atomic properties. *Computer Phys. Commun.* **84**, 37 (1994).

41. Fischer, C. F., Gaigalas, G., Jönsson, P. & Bieroń, J. GRASP2018-A Fortran 95 version of the general relativistic atomic structure package. *Comput. Phys. Commun.* **237**, 184 (2019).

42. Kahl, E. V. & Berengut, J. C. AMBIT: a programme for high-precision relativistic atomic structure calculations. *Comput. Phys. Commun.* **238**, 232 (2019).

43. Träbert, E., Beiersdorfer, P. & Brown, G. V. Observation of hyperfine mixing in measurements of a magnetic octupoledecay in isotopically pure nickel-like ^{129}Xe and ^{132}Xe ions. *Phys. Rev. Lett.* **98**, 263001 (2007).

44. Hosaka, K. et al. Laser spectroscopy of hydrogenlike nitrogen in an electron beam ion trap. *Phys. Rev. A* **69**, 011802(R) (2004).

45. Klein, H. A. et al. Laser spectroscopy of the 2S lamb shift in hydrogenic silicon. *Lect. Notes Phys.* **570**, 664 (2001).

46. Mäckel, V., Klawitter, R., Brenner, G., Crespo López-Urrutia, J. R. & Ullrich, J. Laser spectroscopy on forbidden transitions in trapped highly charged Ar^{13+} ions. *Phys. Rev. Lett.* **107**, 143002 (2011).

47. Schnorr, K. et al. Coronium in the laboratory: measuring the Fe XIV green coronal line by laser spectroscopy. *Astrophys. J.* **776**, 121 (2013).

48. Ralchenko, Y. Infrared and visible laser spectroscopy for highly-charged Ni-like ions. *Nucl. Instrum. Meth. B* **408**, 38 (2017).

49. Kimura, N. et al. 5p-4f level crossing in palladium-like ions and its effect on metastable states. *Phys. Rev. A* **102**, 032807 (2020).

50. Stone, N. J. Table of nuclear magnetic dipole and electric quadrupole moments. *Data Nucl. Data Tables* **90**, 75 (2005).

51. Nakamura, N., Kikuchi, H., Sakaue, H. A. & Watanabe, T. Compact electron beam ion trap for spectroscopy of moderate charge state ions. *Rev. Sci. Instrum.* **79**, 063104 (2008).

52. Soria Orts, R. et al. Zeeman splitting and g factor of the $1s^2\,2s^2\,2p\;^2P_{3/2}$ an $^2P_{1/2}$ levels in Ar^{13+}. *Phys. Rev. A* **76**, 052501 (2007).

53. Tsuda, T. et al. Resonant electron impact excitation of 3d levels in Fe^{14+} and Fe^{15+}. *Astrophys. J.* **851**, 82 (2017).

54. Beiersdorfer, P., Osterheld, A. L., Decaux, V. & Widmann, K. Observation of lifetime-limited X-ray linewidths in cold highly charged ions. *Phys. Rev. Lett.* **77**, 5353 (1996).

55. Kramida, A., Ralchenko, Y., Reader, J. & NIST ASD Team. Nist atomic spectra database (version 5.9). http://physics.nist.gov/asd (2021).

56. Vondrasek, R. On-line charge breeding using ECRIS and EBIS. *Nucl. Instr. Meth. Phys. Res. B* **376**, 16 (2016).

57. Campbell, C. J., Radnaev, A. G. & Kuzmich, A. Wigner crystals of ^{229}Th for optical excitation of the nuclear isomer. *Phys. Rev. Lett.* **106**, 223001 (2011).

58. Safronova, M. S., Safronova, U. I., Radnaev, A. G., Campbell, C. J. & Kuzmich, A. Magnetic dipole and electric quadrupole moments of the ^{229}Th nucleus. *Phys. Rev. A* **88**, 060501(R) (2013).

59. Thielking, J. et al. Laser spectroscopic characterization of the nuclear-clock isomer ^{229m}Th. *Nature* **556**, 321 (2018).

60. Li, Fei-Chen, Qiao, Hao-Xue, Tang, Yong-Bo & Shi, Ting-Yun Relativistic coupled-cluster calculation of hyperfine-structure constants of ^{229}Th^{3+} and evaluation of the electromagnetic nuclear moments of ^{229}Th. *Phys. Rev. A* **104**, 062808 (2021).

61. Porsev, S. G., Safronova, M. S. & Kozlov, M. G. Precision calculation of hyperfine constants for extracting nuclear moments of ^{229}Th. *Phys. Rev. Lett.* **127**, 253001 (2021).

62. Gu, M. F. The flexible atomic code. *Can. J. Phys.* **86**, 675 (2008).

63. Ivanova, E. P. Energy levels in Ag-like ($4d^{10}4f$, $4d^{10}5l$ ($l = 0$-3)), Pd-like ($4d^94f$ [$J = 1$], $4d^95p$ [$J = 1$], $4d^95f$ [$J = 1$]), and Rh-like ($4d^9$ [$J = 5/2, 3/2$]) ions with $Z < 86$. *Data Nucl. Data Tables* **95**, 786 (2009).

64. Egl, A. et al. Application of the continuous stern-Gerlach effect for laser spectroscopy of the ^{40}Ar^{13+} fine structure in a penning trap. *Phys. Rev. Lett.* **123**, 123001 (2019).

65. Draganić, I. et al. High precision wavelength measurements of QED-sensitive forbidden transitions in highly charged argon ions. *Phys. Rev. Lett.* **91**, 183001 (2003).

66. Soria Orts, R. et al. Exploring relativistic many-body recoil effects in highly charged ions. *Phys. Rev. Lett.* **97**, 103002 (2006).

67. Yao, K. et al. M_F-dependent lifetimes due to hyperfine induced interference effects. *Phys. Rev. Lett.* **97**, 183001 (2006).

68. Chantler, C. T., Nguyen, T. V. B., Lowe, J. A. & Grant, I. P. Convergence of the Breit interaction in self-consistent and configuration-interaction approaches. *Phys. Rev. A* **90**, 062504 (2014).

69. Kozioł, K. Breit and QED contributions in atomic structure calculations of tungsten ions. *J. Quant. Spectrosc. Radiat. Transf.* **242**, 106772 (2020).

70. Safronova, M. S., Safronova, U. I., Porsev, S. G., Kozlov, M. G. & Ralchenko, Y. Relativistic all-order many-body calculation of energies, wavelengths, and M1 and E2 transition rates for the $3d^n$ configurations in tungsten ions. *Phys. Rev. A* **97**, 012502 (2018).

71. Angeli, I. & Marinova, K. P. Table of experimental nuclear ground state charge radii: an update. *Data Nucl. Data Tables* **99**, 69 (2013).

72. Andersson, M. & Jönsson, P. HFSZEEMAN-A program for computing weak and intermediate field fine and hyperfine structure Zeeman splittings from MCDHF wave functions. *Comput. Phys. Commun.* **178**, 156 (2008).

73. Li, W., Grumer, J., Brage, T. & Jönsson, P. Hfszeeman95-A program for computing weak and intermediate magnetic-field- and hyperfine-induced transition rates. *Comput. Phys. Commun.* **253**, 107211 (2020).

Acknowledgements

Author contributions

N.K. conceived and initiated this work. N.K., S.K., T.A., and N. Nak. designed the experimental scheme and selected the target ion. N.K. and Priti carried out the LIF measurement using a compact EBIT device developed by N. Nak. Y.K., P. Pip., K.S., and N. Num. provided support for the EBIT operation. The laser system was constructed by N.K. and S.K. The experimental data were analyzed by N.K. and Priti. The theoretical calculation was performed by Priti. N.K. prepared the initial manuscript assisted by Priti, S.K., T.A., and N. Nak. All authors discussed the result and reviewed the manuscript.

Competing interests

The authors declare no competing interests.

Additional information

Supplementary information The online version contains supplementary material available at https://doi.org/10.1038/s42005-023-01127-x.

Correspondence and requests for materials should be addressed to Naoki Kimura.

Peer review information *Communication Physics* thanks the anonymous reviewers for their contribution to the peer review of this work. Peer reviewer reports are available.

Reprints and permission information is available at http://www.nature.com/reprints

Publisher's note Springer Nature remains neutral with regard to jurisdictional claims in published maps and institutional affiliations.